Fatigue initiation mechanisms in elastomers: a microtomography-based analysis

Thomas Glanowski, Bertrand Huneau, Yann Marco, V. Le Saux, Clément Champy, Pierre Charrier

Fatigue initiation mechanisms in elastomers: a micro-tomography-based analysis

Thomas Glanowski[1,*], *Bertrand Huneau*[2], *Yann Marco*[3], *Vincent Le Saux*[3], *Clément Champy*[1] and *Pierre Charrier*[1]

[1]Vibracoustic, CAE & Durability Prediction Department, 44474 Carquefou, France
[2]Institut de Recherche en Génie Civil et Mécanique (GeM), UMR CNRS 6183, Ecole Centrale de Nantes, France
[3]Institut de Recherche Dupuy de Lôme (IRDL), UMR CNRS 6027, ENSTA Bretagne, France

Abstract. The fatigue properties of filled elastomers are strongly related to the population of inclusions induced by their complex recipes and mixing/injection processes. The description and the understanding of the basic damage and dissipation mechanisms involved around these inclusions, the influence of their nature, geometry, size, interface and cohesion properties are especially important to optimize the fatigue design of industrial compounds and parts. The objective of the study is to take advantages of tomography observations to characterize the effects of the 3D inclusions on the fatigue resistance of rubber filled with carbon black. An images processing is necessary to dissociate accurately the inclusions of the matrix. The three dimensional observations provide many information on the inclusion's morphology (size, shape) and their spatial distribution. Moreover, the proposed images processing allows detecting cracks inside and on the surface of the specimen, which offers a better insight on the early stages of the fatigue damage scenario. Then, a numerical model and thermo-mechanical measurements are used to understand why some inclusions become initiation sites. Finally, one activated site is fully described as example.

1 Introduction

The fatigue properties of elastomeric parts are strongly related to the microstructure features (inclusions nature, shape, size, size scattering, spatial distribution) because these reinforced materials are heterogeneous. The industrial development of materials resistant to fatigue is therefore very complex because the parameters driving the microstructure are incredibly numerous, including original ingredients and the processing parameters, from mixing to injection and curing. Inclusions above ten micrometres exert an influence on the fatigue properties of elastomeric compounds. They are commonly estimated with the "Dispergrader" device [1]. More sophisticated technics can be used like micro-tomography [2] to describe the inclusions populations. The accurate description of the initiation sites' morphology [3-7] allows the understanding of the early stages of fatigue damage mechanisms but only from a geometrical point of view. Some recent studies tried to relate thermo-mechanical measurements and micro-tomography analysis to characterize the fatigue properties of elastomeric materials [8, 9]. But the link between macroscopic mechanical criteria and local failure mechanisms are still missing because the main failure mechanisms identified in the literature are only described from a geometrical point of view.

The aim of this study is to understand why some inclusions become an initiation site and others don't. First of all, a tool is developed to provide a full description of the microstructure features such as the shape, the size, and the spatial distribution of inclusions. Then, this microstructural information feeds simulations in order to evaluate the criticality of inclusions properties. Finally, the case of one inclusion is presented and a thermo-mechanical experimental protocol is defined to assess the response at the inclusion scale.

2 Tools for the description of the inclusions and cracks population

2.1. Material and specimen

The material studied is a fully formulated natural rubber reinforced with carbon blacks. Classic hourglass samples (Figure 1) are used to characterize fatigue damage scenarios. These samples are injected and representative of the manufacturing process used for automotive anti-vibration parts.

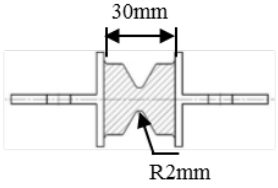

Fig. 1. Geometry of the AE2 hourglass sample.

* Corresponding author: thomas.glanowski@vibracoustic.com

2.2 Motivations for using X-ray computed micro-tomography

Micro-tomography is a remarkable tool to provide a non-destructive internal observation. This method is widely used for the study of materials microstructure [10] including rubber [4]. Compared with usual 2D analysis methods such as the scanning electron microscope, the 3D reconstruction of the microstructure by micro-tomography grants to:

- Quantify statistically the number, size, shape and orientation of objects;
- Study the spatial distribution of objects;
- Avoid artefacts due to cutting and surface preparation for 2D observations.

However, the micro-tomography has some drawbacks:

- The resolution is about a few micrometre (much lower than that SEM);
- The possibly duration of acquisition;
- The huge size of the result files;
- Lack of access to the chemical composition (unlike SEM with EDS probe).

Furthermore, the X-ray micro-tomography is an excellent tool to follow 3D damage evolution [4]. The samples of the study were analysed with the X-Radia XCT micro-tomograph, located at Ecole Centrale de Nantes (GeM). A quite high resolution is reached with a voxel size at 8.32µm. The specimen is slightly stretched to open the cracks.

2.3 Images processing

Many software are available to process and visualize 3D micro-tomographies, such as Avizo3D, myVGL, Paraview and ImageJ. However, our choice was to use the Python programming language which is widely used in the scientific world and can provide account to more specific developments. Indeed, the use of a programming language for tomography processing allows finer control and more complex analysis possibilities. Gouillart et al. [11] show the ability of Python and the scikit-image library to analyse micro-tomography data.

The goal of the images processing is the segmentation of the different types of inclusions in the material. The segmentation consists of partitioning the tomography into several regions, in which the voxels satisfy a certain homogeneity criterion, based for example on the gray level. The segmentation algorithm must minimize the loss of information on the microstructure caused by the simplification of the images, due to the different transformations applied. Thus, segmentation remains a difficult step since the choice of the segmentation algorithm can lead to significant differences in the morphological characterization of the microstructure. The algorithms used to segment regions of interest depend on the properties of the images. They can be classified in different families such as the thresholding algorithms, the super pixel algorithms [12], the region growing algorithms [13] and the active contour algorithms [14]. Thresholding methods are the most common. They use the histogram data of the images. The threshold gray level is chosen manually or automatically to select the objects of interest. These techniques consider voxels independently and don't use consistency with their neighbors. These techniques are effective when the objects and the background have two distinct peaks on the grayscale histogram.

2.3.1 Pre-treatment

An exposure adjustment is done in order to increase the contrast and delete extreme values due to experimental noise. Then, a 3D median filter is applied to make the segmentation easier afterwards. It reduces noise while preserving edges.

2.3.2 Cracks segmentation

A thresholding operation is applied to the sample in order to separate it from the background. Then, it is necessary to reconstruct the specimen without cracks in order to make the segmentation of cracks. Mathematical morphology operations are applied to fill inner cracks. The outer cracks are filled with an active contour method [14]. Finally, a subtraction of the reconstructed sample from the sample obtained after threshold is done to have only cracks. The Figure 2 shows the cracks detected on one slice of the micro-tomography.

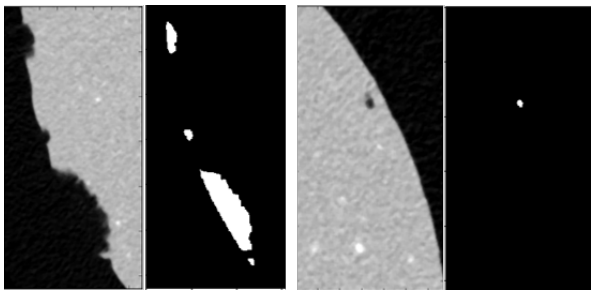

Fig. 2. Cracks segmentation on the sample's surface (left) and inside the specimen (right).

2.3.3 Inclusions segmentation

The thresholding method is not used for the inclusions segmentation because the chosen value has a strong influence on the size of the biggest detected inclusions. Thus, in order to have an accurate inclusions segmentation, a 3D region growth algorithm that combines information on the value of the gray level and the position of the voxels is used [13]. First of all, the user defines markers labeling regions of the image belonging to the inclusion or to the matrix. Some regions remain indeterminate like highlighted in the Figure 3. Then, an anisotropic diffusion equation is solved with tracers initiated at the marker's position. The local diffusivity coefficient is greater if neighboring voxels have similar values, so that diffusion is difficult across high gradients. The label of each unknown voxel is set to the label of the known marker that has the highest

probability to be reached first during the diffusion process. This algorithm needs one parameter which controls the split between the two phases. Then, only inclusions above 30µm are kept. However, this size is relevant for the study of the fatigue properties, considering that the most critical inclusions for the enforced fatigue loading are those which size exceeds 20 to 40µm.

Fig. 3. Inclusions segmentation steps: denoised data (left), markers (center), result of the algorithm superposed to the denoised data (right).

Thanks to this segmentation method, the size of the biggest inclusions is insensitive to the user defined markers (see Figure 3). The Figure 4 shows on one slice the result of the inclusions segmentation. All detected inclusions have their outline drawn.

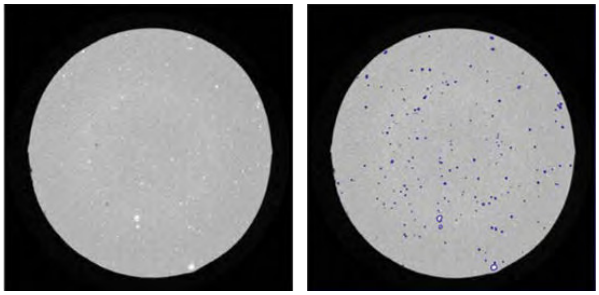

Fig. 4. Result of the inclusions' segmentation: denoised image (left), inclusions detected (right).

2.4 Statistical treatment of inclusions

The segmentation give a binarized matrix of regions of interests. The characteristic of each labelled region can be measured. The boundary between the inclusion and the background is approximated with a triangular representation, obtained from the Lewiner marching cube algorithm [15]. According to Nyström et al. [16], the estimations of the volume and the surface area are more accurate with the triangular representation than the voxelized representation of the inclusions. The statistical post treatment is made on about 5 000 inclusions.

2.4.1 Inclusions' size

A first microstructural indicator is the size of the inclusion. The equivalent diameter of a sphere with the same volume as the labelled region is used.

2.4.2 Inclusions' shape and orientation

The shape of inclusions can be assessed with a compactness factor CF, function of the surface area A and the volume V:

$$CF = \frac{\pi^{1/3}\,(6V)^{2/3}}{A} \quad (1)$$

The shape factor expresses the sphericity of the inclusion: in the case of a perfect sphere, it is equal to 1, otherwise $CF<1$. The shape factor gives a good evaluation of the inclusions' shape, but is strongly dependent of the voxel size. To solve this issue, the optimal ellipsoid with the smallest volume enclosing all voxels is calculated [17] (Figure 5). The surface area and the volume can be calculated on this ellipsoid. Furthermore, the orientation of the inclusions in the sample can be obtained.

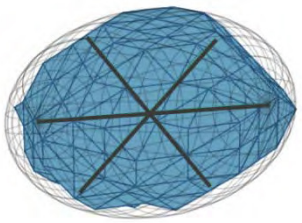

Fig. 5. Best ellipsoid found with its axis for an inclusion meshed with triangles.

2.4.3 Inclusions' spatial distribution

In the following, the inclusions are considered only by their centroid. Several methods are used to study the spatial distribution of inclusions. The first one can be the measurement of the nearest neighbour spacing distribution. This method is able to describe the inclusions distribution as being ordered, random, clustered or composed of clusters superimposed on random inclusions distribution. However, it is not a very sensitive method for clusters evaluation since only the nearest neighbour is detected. No description of the cluster size and spacing can be provided. Another method often used to assess the spatial distribution is the K-function of Ripley [18]. This function is the average number of inclusions in a sphere of radius r, centered on each inclusion. The K-function is reasonably sensitive to local disturbance of inclusions pattern and is able to characterize inhomogeneous population of points as well as mixture of several types of point's pattern [19].

2.5 Observed initiation mechanisms

The segmentation data of the inclusions and of the cracks are superposed in order to observe the damage mechanism. This analysis exhibits two types of damage

mechanisms. The first one is the cavitation at the poles of the inclusion. The other type of damage mechanism is the failure of inclusions (see Figure 6).

Fig. 6. Damage mechanism observed: cavitation at the pole (left) and failure of the inclusion (right).

3 Tools for the definition of a local criterion

3.1. Criticity of inclusion

A detailed study on the initiation of fatigue cracks in carbon black filled natural rubber was done by Huneau et al. [5]. The criticity of inclusions are assessed thanks to the scanning electron microscope observations of interrupted fatigued samples and fatigue fracture surfaces. The use of the scanning electron microscope, coupled with energy dispersive spectrometry of X-rays, enables the analysis of the chemical nature of inclusions detected as activated sites. The study highlights that fatigue damage generally initiates on carbon black agglomerates or on metallic oxide such as ZnO. However, those two types of inclusions generate different crack initiation mechanism. It is shown that the ones on carbon black agglomerates are almost always followed by a crack propagation leading to the failure of the sample. A possible explanation is that carbon black agglomerates have a stronger cohesion than ZnO and a stronger adhesion to the matrix.

In our study, the inclusions detected by the image processing are composed of metallic oxide and of inclusions called “bumps” (Figure 7). This last type of inclusion is an agglomerate of rubber, carbon black and zinc oxide according to the energy dispersive spectrometry of X-rays analysis.

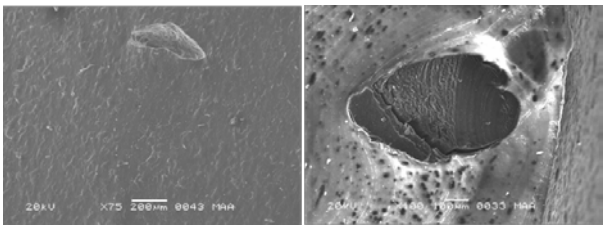

Fig. 7. Scanning electron microscope observation of the inclusions called “bumps”.

It was observed with the same method than used in Huneau et al. [5] that “bumps” are possible initiation sites that can lead to failure. More precisely, we observed a cavitation process at the pole of the inclusion in this case as described in the study of Saintier et al. [20]. The cavitation is the process of void nucleation under a given stress state. In our study, it was also observed that ZnO are initiation sites but the created cracks don’t propagate. In order to understand, why some inclusions initiate and others don’t, we used some simple finite element model and temperature measurements.

3.2 Determination of a local criterion

3.2.1 Simulation tool

A parametric finite element study can be carried out in order to understand the influence of inclusions parameters such as the type, the size, the shape, the inclusions spacing on the fatigue resistance. The simulations are fed with the micro-tomography results found in the previous section. A cylindrical cell is considered with a central ellipsoidal inclusion. Due to symmetry, only a quarter of the cell is considered (Figure 8). The radius of the cell used is set according to the micro-tomography results giving account of the average distance to the nearest inclusion. The size of the inclusion considered is the average of the equivalent diameter of all inclusions detected by the image processing.

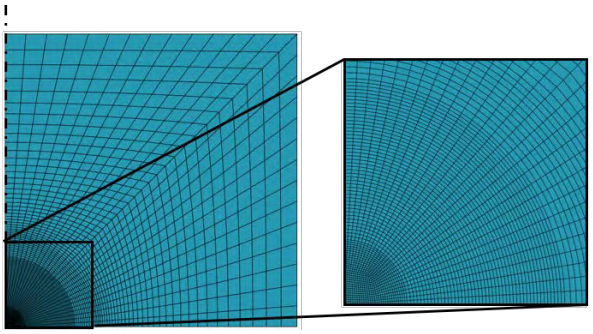

Fig. 8. Axisymmetric finite element model of a cylindrical cell with a central ellipsoidal inclusion.

The nodal displacement of the upper part is imposed and the lateral border of the cell verifies the periodicity hypothesis. A Neo-Hookean behaviour law is used. The hyperelastic potential parameters are identified on the stabilized tensile behaviour of the material using a specific protocol applied on AE2 samples. The transposition of constitutive models and failure criteria from the macroscopic scale to microscopic scale seems possible [21]. The failure criteria used here is related to the cavitation process. Hou and Aberyartne [22] established a cavitation criterion defined for multiaxial loading with a cavitation surface. Considering a Neo-Hookean behaviour law this criterion is written:

$$S: (4\sigma_1 - \sigma_2 - \sigma_3)(4\sigma_1 - \sigma_2 - \sigma_3)(4\sigma_1 - \sigma_2 - \sigma_3) - (5\mu)^3 = 0 \quad (1)$$

with σ_1 , σ_2 , σ_3 the principal stresses and μ the shear modulus. In this study, it is not expected to give an

accurate prediction of the strain and stress level that leads to cavitation. The use of this criterion aims at assessing the criticity of inclusion parameters. We considered that the interface between the inclusion and the matrix is perfect.

The first studied parameters are the shape and the Young's modulus of the inclusion. According to micro-tomography results, most of inclusions have a compactness factor between 0.9 and 1, so the inclusions are close to spherical object. Therefore, we define three ellipsoidal inclusions with the same volume (see Figure 9). The sphere, the oblate ellipsoid and the prolate ellipsoid have respectively compactness factor of 1, 0.93 and 0.91 The description of these three ellipsoids can also be done thanks to the shape factor *f* defined by: $f = a/b$. In order to evaluate the influence of the shape and of the Young's modulus on the cavitation, we considered the strain needed to reach the cavitation criterion (see Equation 1).

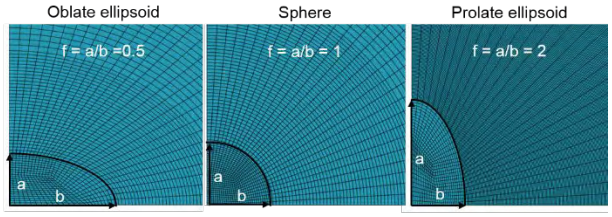

Fig. 9. Ellipsoids considered to study the influence of the shape on the cavitation.

The results show that the cavitation is localized above the inclusion in the spherical and prolate ellipsoid. For the oblate ellipsoid, the cavitation is close to the inclusion's interface. Whatever the shape of the inclusion, an increase of the Young's modulus induces a decrease of the strain leading to cavitation (Figure 10). A low strain value leading to cavitation means a poorer fatigue properties of the compound. In our material, the inclusion can be considered as fully rigid compared to the elastomeric matrix above a Young's modulus of 500MPa. We observe no evolution of the strain at cavitation for a higher value of Young's modulus. This effect of the Young's modulus can be explained easily by the less stiff inclusion and the lower stress values [23]. Regarding the inclusion's shape, the most critical inclusion is the prolate ellipsoid (*f=2*). If we consider a fully rigid inclusion, the strain at cavitation is reduced of 38% in the case of a prolate ellipsoid compared to a sphere. Moreover, the increase of the Young's modulus on prolate ellipsoid has more effect than for the sphere and oblate ellipsoid cases. The oblate ellipsoid is the less critical for the cavitation phenomenon. However, due to the location of the cavitation at the inclusion's interface, this shape of inclusion could be the most critical if a debonding criterion is used.

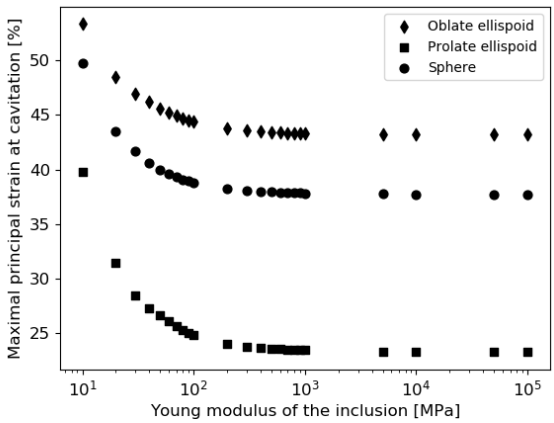

Fig. 10. Effect of the inclusion's size and Young's modulus on the cavitation.

Furthermore, the influence of the size of the three ellipsoidal inclusions is studied. The Young's modulus is fixed at 1GPa. Thus, the inclusion is fully rigid compared to the elastomeric matrix. The Figure 11 shows that the most critical inclusion is always the prolate ellipsoid whatever its size. The increase in size induces a decrease of the strain at cavitation.

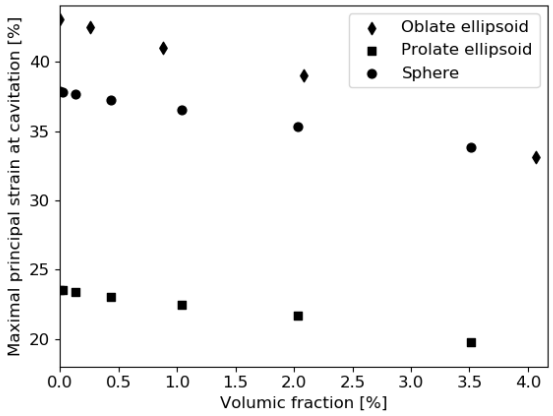

Fig. 11. Effect of the inclusion's size and shape on the cavitation.

Finally, we focus on the effect of the distance between two inclusions. The range of distance between inclusions is determined thanks to the evaluation of distance to the nearest neighbour inclusion. In average, the inclusions' centroids are separated by 245µm. The shortest distance between two inclusions is 32µm. Figure 12 highlights the axisymmetric model used to assess the spherical inclusions inter-distance effect. We considered only the most critical case where inclusions are aligned along the tensile direction. The size of the sphere is determined as the average size of inclusions detected by micro-tomography.

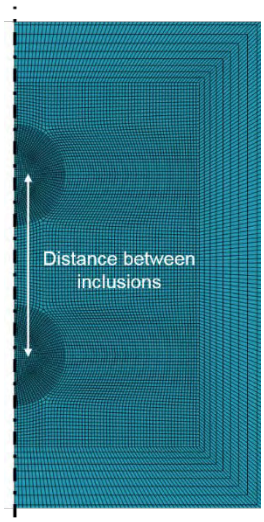

Fig. 12. Finite element model considered for two spheres aligned in the tensile direction.

Figure 13 shows that the proximity of two inclusions in the tensile direction can decrease dramatically the strain at cavitation. For a distance above 225µm, the inclusion has no more effect on the other one for this average size of inclusions. Thus, in the case studied here, few inclusions have influence on each other.

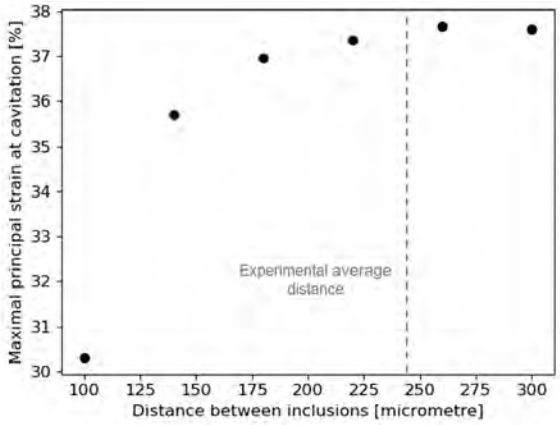

Fig. 13. Effect of the distance between inclusions on the cavitation.

3.2.2 Experimental tool

The thermo-mechanical observations at the scale of inclusions can help to characterize the early stages of the fatigue damage scenario. The experimental approach is fully detailed in a previous communication [21]. Only the main points are recalled here.

The tests are achieved on a Bose electro-dynamical testing machine equipped with a 3.2kN load cell and are displacement controlled. The thermal acquisition is performed thanks to a FLIR SC7600-BB infrared camera with the so-called "G1" lens with an analyzed zone of 7mm*5mm. the thermal resolution is improved with a pixelwise calibration taking into account the housing temperature [24].

The sample is submitted to succession of cyclic sinusoidal loading blocks increasing displacement amplitudes. Each block is composed of an accommodation stage (10 cycles at 30Hz) to stabilize the Mullins effect. Then, the sample is kept to the maximal deformation during cooling to return to thermal equilibrium. Finally, the thermal acquisition is performed using a rate of 200 frames/s, during the loading step (50 cycles at a mechanical frequency of 30Hz).

The evaluation of the thermal sources from the temperature measurements requires solving the heat equation. The way to obtain the dissipated energy from the temperature is explain in another study [25].

4 Example on one activated site

4.1. Infrared response and micro-tomography of one activated site

An initiation site in the AE2 sample was observed with the infrared measurement. The acquisition of the thermal response of the inclusion was obtained during the heat build-up test (Figure 14).

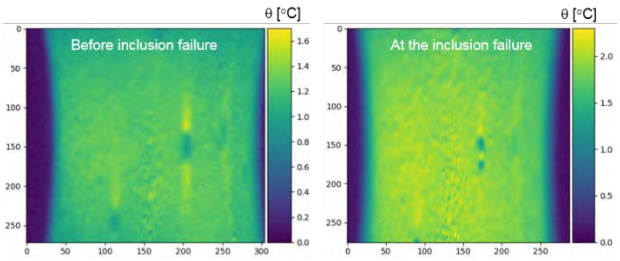

Fig. 14. Infrared measurement before (left) and after (right) the activation of the site.

After the activation of the site, it was observed by micro-tomography and optical microscopy. It was noticed that the inclusion is localized below the surface of the sample (Figure 15).

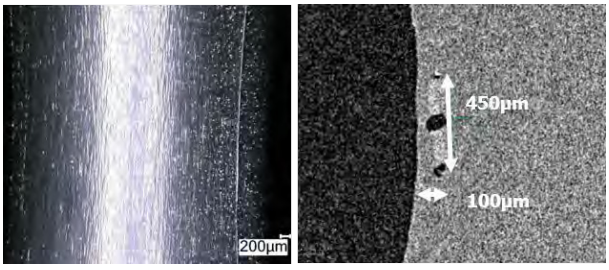

Fig. 15. Observations of the sample with a numerical microscope (left) and with micro-tomography (right).

4.2. Comparison of the infrared measurement with the simulation

To predict the dissipated energy, Le Chenadec et al. [26] model can be used. This approach is based on the idea to relate the cyclic hyperelastic energy to the dissipated

energy. Le Saux et al. [27] showed the efficiency of this model to describe and predict the temperature and energy fields for various loading conditions of macroscopic samples. Moreover, Masquelier et al. [25] illustrated the ability of this approach to give a good correlation between the experimental and simulated fields. The parameters of this model are identified on the AE2 sample [28]. We are using this energetic model in order to evaluate the dissipated energy of this inclusions numerically. The comparison between experimental and finite elements simulation enables to challenge the experimental analysis protocols and opens the way to the validation of microscopic failure criteria.

5 Conclusion

This paper presents the approach developed to better understand and describe the early stages of the fatigue damage scenarios. The micro-tomography and the image processing used enable to have quantitative 3D information on the size, shape and spatial distribution of inclusions in the material. This information feeds simulations in order to better understand the impact of some inclusion's parameters on the cavitation phenomenon. As expected, it was shown that the parameters such as the Young's modulus and the shape have a strong influence on the strain leading to cavitation and thus on the fatigue properties. This study has to be pursued by taking into account the quality of the interface between the matrix and the inclusion.

The authors would like to thank the ANRT for its financial support and all the partners of the PROFEM 2 project, Vibracoustic, GeM, IRDL and François Bertrand (GeM) for providing micro-tomography images.

References

1. S. Persson, *Polymer Testi*ng **4**, 45 (1984)
2. K. Le Gorgu Jago, ECCMR V, 173-177 (2008)
3. A. N. Gent and B. Park, *Journal of Materials Science* **19**, 1947-1956 (1984)
4. K. Le Gorgu Jago, *Rubber Chemistry Technology* **85**, 387-407 (2012)
5. B. Huneau, I. Masquelier, Y. Marco, V. Le Saux, S. Noizet, C. Schiel and P. Charrier, *Rubber Chemistry and Technology* **89**, 126-141 (2016)
6. J. B. Le Cam, B. Huneau and E. Verron, *International Journal of Fatigue* **52**, 82-94 (2013)
7. V. Le Saux, Y. Marco, S. Calloch and P. Charrier, *Polymer Eng. and Science* **51**, 1253-1263 (2011)
8. V. Le Saux, Y. Marco, S. Calloch, C. Doudard and P. Charrier, *Int. J. Fatigue* **32**, 1582-1590 (2010)
9. Y. Marco, I. Masquelier, V. Le Saux, S. Calloch, B. Huneau and P. Charrier, *ECCMR VIII* (2013)
10. L. Salvo, P. Cloetens, E. Maire et al., *Nucl. Intrum. Meth.* **200B**, 273-286 (2003)
11. E. Gouillart, J. Nunez-Iglesias and S. van der Walt, *Adv. Struct. Chem. Imag.* (2018)
12. P.F. Felzenswalb, D. P. Huttenlocher, *International Journal of Computer Vision* **59**, 167-181 (2004)
13. L. Grady, *IEEE Trans. Pattern Analysis and Machine Intelligence* **28,** 1768-1783 (2016)
14. M. Kass, A. Witkin, D. Terzopoulos, *International Journal of Computer Vision* **1**, 321-331 (1988)
15. T. Lewiner, H. Lopes, A. Vieira and G. Tavares, *Journal of Graphic Tools* **8**, 1-15 (2003)
16. I. Nyström, J. K. Udupa, G. J. Grevera and B.E. Hirsch, *Medical Imaging 2002: Visualization, Image-Guided Procedures Display* **4681**, 669-680 (2002)
17. N. Moshtagh, *Convex Optimi*zation., 111-112 (2005)
18. B. D. Ripley, *Journal of the Royal Statistical Society* **39**, 172-212 (1977)
19. R. Pyrz, *Mechanics of Microstructural Materials*, 173-233 (2004)
20. N. Saintier, G. Cailletaud, R. Piques, *International Journal of Fatigue* **28**, 61-72 (2006)
21. T. Glanowski, Y. Marco, V. Le Saux, B. Huneau, C. Champy, P. Charrier, ECCMR X, 341-346 (2017)
22. H. Hou and R. Abeyaratne, *J. Mech. Phys. Solids* **92**, 571 (1992)
23. N. Saintier, PhD, 2001
24. V. Le Saux, C. Doudard, Infrared Physics and Technology **80**, 83-92 (2017)
25. I. Masquelier, Y. Marco, V. Le Saux, S. Calloch, P. Charrier, Mechanics of Materials **80**, 113-123 (2015)
26. Y. Le Chenadec, I. Raoult, C. Stolz, M. Nguyen-Tajan, Mech. Material Structure **4**, 309-318 (2009)
27. V. Le Saux, Y. Marco, S. Calloch, P. Charrier and D. Taveau, *Rubber Chem. Techn.* **86**, 38-56 (2013)
28. T. Glanowski, V. Le Saux, C. Doudard, Y. Marco , C. Champy, P. Charrier, Continuum Mechanics and Thermodynamics **29**, 1163-1179 (2017)